Analysis of Unsteady Viscous Flow Past an Airfoil: Part II—Numerical Formulation and Results

Zygmunt M. Cielak* and Robert B. Kinney†
University of Arizona, Tucson, Ariz.

A numerical formulation of the analysis presented in Part I is developed. The integral equation for the bound-vorticity distribution is cast into a system of linear simultaneous equations. The unsteady vorticity transport equation is solved in finite-difference form using a standard technique which is explicit in time. A semianalytical procedure is developed for the calculation of the velocity field via the Biot-Savart law. The utility of the numerical method is demonstrated through calculations performed for the flow past a symmetrical Joukowski airfoil impulsively set into motion. The airfoil thickness is approximately 12%, and results are presented for angles of attack of 0 deg and 30 deg for a Reynolds number of 400. Representative vorticity contours, velocity profiles, and pressure distributions over the airfoil surface are given. An important feature of the method is that the pressure distribution is inherently single-valued, this being calculated directly from an integral of the bound-vorticity distribution over the surface. The precision of the results is found to be quite good, even near the cusped trailing edge.

Nomenclature

C_P = pressure coefficient, Eq. (8)
K = kernel function in velocity induction law
P = static pressure
Re = Reynolds number
ΔS = surface increment on the airfoil
$\dot{S}$ = shape parameter for the airfoil surface, Eq. (4)
Δt = time increment
U = velocity of the undisturbed onset flow relative to the airfoil
u = velocity component in ξ direction
x = Cartesian coordinate measured along the chord from the midpoint
y = Cartesian coordinate perpendicular to chord
z = complex variable, $x+iy$
α = angle of attack
γ = bound-vorticity distribution
η = body-oriented coordinate measured perpendicular to airfoil surface
ζ = complex variable in Joukowski transformation, Eq. (1)
θ = slope angle of airfoil surface relative to the chord
ξ = body-oriented coordinate measured along the airfoil
ρ = fluid density
ϕ = polar angle measured from the real axis in the transformed (circle) plane

Introduction

WITH few exceptions, two-dimensional finite-difference solutions to the unsteady Navier-Stokes equations are based on the vorticity-stream function approach. The flowfield and solid boundaries are covered with a system of node points, and discretized versions of the stream-function and vorticity-transport equations are solved simultaneously at each point. Enforcement of the no-slip condition at solid boundaries generates a relationship between the wall values for the vorticity and stream function, the former being an unknown. Since the numerical solution of the coupled equations requires that the wall vorticity be specified at boundary points, the calculations for each time step are often performed iteratively until all of the equations and wall conditions are satisfied simultaneously.

The present formulation, as developed in Part I,[1] departs markedly from that described in the foregoing. Although the (free) vorticity is still a fundamental variable, the treatment of the boundary condition at solid surfaces is entirely different. Specifically, in the present work the vorticity production is prescribed rather than the wall vorticity. Recalling that in two dimensions there is an analogy between heat and vorticity transport, the present wall boundary condition is analogous to prescribed wall heat flux rather than prescribed wall temperature. The release of free vorticity to the fluid is locally variable along the solid surface and is in just such measure that the no-slip condition is satisfied at each instant in time. In addition, a global conservation principle is invoked which insures that the total vorticity in the fluid remains zero at all times.

A further departure arises in the calculation of the velocity field. This is obtained from kinematic principles based on the Biot-Savart law. In addition to the velocity induced by the free-vorticity field, the contribution from the distribution of bound-vortex singularities, which replace the solid surface, must also be taken into account. These are so constituted that the normal velocity component at points on the solid surface is identically zero at all times.

In this part of the paper, the numerical formulation is developed in detail. Numerical results are also presented for the unsteady flowfield produced by a symmetrical Joukowski airfoil impulsively set into motion in a viscous fluid. No attempt has been made to carry the calculations to large time values. Rather, the intent has been only to generate sufficient results that the utility of the method can be demonstrated.

Numerical Formulation

Calculation of Bound-Vorticity Distribution

The complex transformations given by

$$z=\zeta+(l^2/\zeta) \tag{1}$$

maps a circle in the ζ plane into a Joukowski airfoil in the z plane. Taking a circle of radius $(1+\epsilon)l$, the center of which is

Received July 12, 1976; revision received Aug. 24, 1977.

Index categories: Viscous Nonboundary-Layer Flows; Nonsteady Aerodynamics.

*Research Associate. Presently with Celco Tool and Engineering, Franklin Park, Illinois.

†Associate Professor of Aerospace and Mechanical Engineering. Associate Fellow AIAA.

on the real axis a distance ϵl to the right of the origin, one obtains a symmetrical airfoil. Specifying $\epsilon = 0.1$ and $l = 0.2479$ yields a unit chord length and approximately a 12% thickness.

The entire outline of the airfoil was approximated by a total of 80 discrete segments. Of these, 40 were placed on the top and 40 on the bottom, their arrangement being symmetrical about the chord. A surface point was then positioned at the center of each segment, and a value γ_i $(i = 1,2,\ldots,80)$ was assigned to each point (hereafter referred to as a vortex point).

An equation for γ_i can now be obtained following a procedure similar to that leading to Eq. (5) of Part I. If the segments are assumed to be straight lines with constant slope-angle, the result is

$$\frac{\gamma_i}{2} - \frac{1}{2\pi} \sum_{\substack{m=1 \\ m \neq i}}^{80} \left[\int_{\Delta S_m} \gamma_m K_m(x_i, y_i)\, d\xi \right] = -[\cos(\alpha - \theta_i) + u_{\omega i}] \tag{2}$$

where

$$K_m(x_i, y_i) = \frac{(y_i - y_m)\cos\theta_i - (x_i - x_m)\sin\theta_i}{(y_i - y_m)^2 + (x_i - x_m)^2} \tag{3}$$

and $u_{\omega i}$ is obtained from a numerical integration of Eq. (1a), Part I. This step will be discussed more fully at a later point. Note that in Eq. (2), the ith point is excluded in the summation since the contribution of γ_i to the tangential velocity at the ith point is given by the leading term on the left-hand side.

Interpolation formulas were written for the γ's between surface points, and these were substituted into the individual integrals over the surface segments ΔS_m, appearing in Eq. (2). A linear variation was assumed to exist between all points except the two nearest the trailing edge. This region was treated in the following manner.

No vortex point coincided with the trailing edge $(x = 0.5)$. Rather, the two points on the upper and lower surfaces nearest the trailing edge were positioned at $x = 0.499229$. This is the preferred arrangement, since although γ is singular at $x = 0.5$ (for angle of attack α not equal to zero), the integral of γ exists up to and including the trailing edge. The integral of γ over the rearward half of each ΔS terminating at the trailing edge was approximated by the product of $\Delta S/2$ and the value of γ obtained at the midpoint. Although this underestimates the integral, more complicated extrapolation procedures yielded no noticeable differences in the end results. Furthermore, this is an extremely good approximation when $\alpha = 0$. Therefore, it was used for all of the calculations.

Equation (2) was applied to each of the surface points, and the integrals appearing therein were evaluated analytically. This resulted in 80 simultaneous equations for the γ's. These are too lengthy to give here, but they can be deduced from the relationships given in Appendix C of the dissertation[2] on which this paper is based. The resulting system of equations was then solved by standard means.

The solution to the system of linear equations yields a particular solution only. As shown in Part I, the complete solution must include the complementary solution to the homogeneous equation. The final result can be written as

$$\gamma_i = (\gamma_i)_{\text{part}} - \frac{1}{2\pi \dot{S}_i} \sum_{m=1}^{80} (\gamma_m)_{\text{part}} \Delta S_m \tag{4}$$

In the foregoing, $\dot{S}_i = \sqrt{\dot{x}_S(\varphi_i)^2 + \dot{y}_S(\varphi_i)^2}$, where φ is the polar angle in the (circle) ζ plane, and x_S and y_S are the Cartesian coordinates of the airfoil surface points in the physical plane. To a high degree of approximation,† $\dot{x}_S(\varphi_i) \cong -0.5 \sin\varphi_i$. Also $\dot{y}_S(\varphi_i) = (dy/dx)_S \cdot \dot{x}_S$. The value of $(dy/dx)_S$ was computed from an explicit relationship obtained analytically for this particular Joukowski airfoil.

A comparison between the numerically obtained bound-vorticity distribution and the exact analytical result was made for the case of pure potential flow with zero circulation about the airfoil at 30-deg angle of attack. When plotted on graph paper, the numerical values were nearly indistinguishable from the exact results, even near the trailing edge where γ approaches negative infinity. Nevertheless, it was decided to force exact agreement for this case. This was achieved by calculating "adjusted" values for each of the 80 $\dot{S}_i$'s, such that when these were substituted into Eq. (4), the values of γ_i obtained numerically agreed precisely with the exact result. The corrected values for $\dot{S}_i$ were then used in all future calculations.

To verify that the adjustments in $\dot{S}_i$ were due to discretization errors inherent in Eqs. (2) and (4), additional calculations were made for the case of zero circulation with $\alpha = 5$, 15, and 20 deg. The corrected values for $\dot{S}_i$ found for 30 deg were used in all the numerical evaluations of γ_i for each of the three values of α. The differences between the exact and numerical values were insignificant. Thus, it was concluded that the corrections were not sensitive to the location of the rear stagnation point, and were due instead to geometrical and numerical inaccuracies. For the case $\alpha = 0$, the correction procedure was not required since the complementary solution is identically zero. Moreover, the particular solution for that case was already in excellent agreement with the exact result.

Calculation of Free Vorticity Distribution

A system of control volumes (fluid cells) was constructed over the flowfield using the body-oriented coordinates ξ and η. A scale drawing of the arrangement near the leading and trailing edges is shown in Fig. 1.

The cells immediately adjacent to the airfoil are of a uniform height, equal to $\Delta\eta_0 = 0.02$. The heights of the cells then increase away from the airfoil according to the expansion factor 1.15. Node points are positioned at the midheight of each cell and at a value of ξ which corresponds to the midpoint of the control surface which coincides with the airfoil surface.

A total of 800 control volumes was used to cover the viscous region of the flowfield. Forty cells were in contact with the airfoil surface (20 on the top and 20 on the bottom). There were ten layers of control volumes positioned laterally above and below the airfoil. The region behind the airfoil contained half the control volumes, and these increased in width behind the airfoil according to the expansion factor 1.14. The node points extended to a distance of 0.371 (fraction of the chord) on each side of the airfoil as well as upstream of the leading edge. The extreme downstream node was approximately two chord lengths behind the trailing edge.

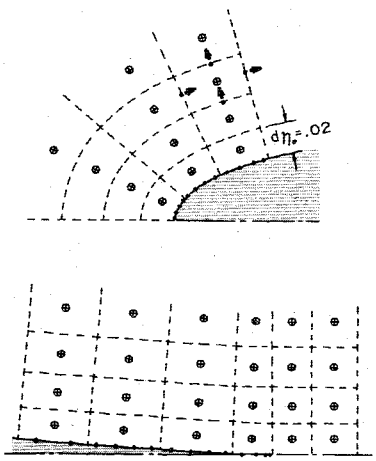

Fig. 1 Scale drawing of node arrangement near leading and trailing edges.

†This expression for $\dot{x}_S$ is exact for the flat-plate and elliptical airfoils. It is so nearly correct for the present Joukowski airfoil that the use of the more complicated exact expression is unnecessary.

A discretized representation of the vorticity transport equation, Eq. (9) in Part I, was obtained from a vorticity balance performed on each control volume. This resulting equation is quite standard and will not be given here. Only the basic approach will be described. The standard forward-in-time explicit representation for the time derivative was used. For the vorticity balance, the finite dimensions of each of the 800 control volumes (i.e., the lengths of the four control surfaces and the areas of each cell) were needed. These were computed at the outset and stored.

The velocity components were needed at the four control faces of each cell. These are shown as the solid arrows for one of the cells in Fig. 1, and they were obtained directly as follows. The velocities in the ξ direction were first calculated at the midpoints of the control surfaces from a numerical integration of the Biot-Savart law, Eq. (1a) of Part I. This step will be explained more fully in the next section. Note that these velocities were not computed at the central node points and then interpolated to obtain the values at the control faces. The components in the η direction were obtained from the continuity equation, once those in the ξ direction were known. Since the velocities can take on positive and negative values, the vorticity transported by the fluid was always taken to be that at the "upwind" node.

The fluid cells adjacent to the airfoil needed special consideration since enforcement of the no-slip condition requires that free vorticity enter the cells across each of the lower control surfaces in contact with the airfoil. The flow of free vorticity across a surface segment of length ΔS_m in time Δt was taken to be $\gamma_m \Delta S_m$. The arrangement of vortex points on the surface was such that the length of the lower control surface of each *fluid* cell was an even multiple of these ΔS_m's. Referring to Fig. 1, it can be seen that in the leading- and trailing-edge regions, there are four such vortex points per fluid cell. This number decreases to 2 and then becomes 1 over most of the airfoil surface.

To illustrate the manner in which the surface boundary condition is incorporated into the numerical solution for the free vorticity let us consider the sequence of events following the impulsive start of the airfoil at 30 deg angle of attack. Immediately after the impulsive acceleration, $t = 0^+$, the free vorticity is everywhere zero, and the bound-vorticity distribution is that corresponding to zero circulation. This is shown in the central part of Fig. 2. The points were obtained numerically from Eq. (2) using the scheme already described. Note that for this step, $u_\omega = 0$. The solid curve is the exact solution obtained from the surface slip velocity calculated from potential-flow theory. In an inset to the figure, the distribution of the velocity component in the ξ direction is shown at a location near the maximum thickness of the airfoil (as indicated by the arrow). The dashed curve corresponds to the potential-flow velocity distribution. We now look at the situation at the end of one time increment, Δt. To advance the solution in time using the explicit technique, the transport of free vorticity between fluid cells is calculated at the previous time level, which in this case is $t = 0^+$. Since the fluid vorticity is everywhere zero, vorticity transport occurs only across the airfoil surface. At the end of the time step, the new vorticity which has entered the fluid is assumed to be uniformly distributed over each fluid cell in contact with the airfoil.

To complete the calculation cycle the new velocity field is calculated using the following procedure:

1) The new free vorticity now in the fluid is used to calculate the contribution, u_ω, to the nonhomogeneous term in Eq. (2), using the Biot-Savart law.

2) A new distribution for γ is then obtained from the system of linear equations, Eq. (2).

3) This new distribution for γ, plus the values of ω already in the fluid cells, are then used to find the u velocity (via the Biot-Savart law) at various points in the fluid. The v velocity is obtained from the continuity equation.

The results of the u-velocity calculation obtained in step 3 are shown as the solid circles in the inset to Fig. 2. Results for only one location along the airfoil are shown (see arrow). To be noted is the fact that a displacement effect has already developed in the external stream, even after one time step. Also, the velocity at the wall after one time step is not quite zero. In fact, it is approximately equal to 0.018. This means simply that at the end of the first time step, the adherence condition is not quite satisfied. Thus, new free vorticity must be produced during the next time step. Note that since there is also free vorticity in the fluid, its transport by convection and diffusion must now be taken into account.

Calculation of Velocity Field

Consider some node point Q in the fluid with vorticity ω, and the corresponding point P at some other location in the fluid, including the airfoil surface, at which the u velocity is to be found. About the point Q, a substitute cell is constructed which has the same height $\Delta\eta$, is positioned the same relative to the center node point, and has the same areas as the actual fluid cell, but which is rectangular in shape. Except for a very few cells near the leading edge, the rectangular shape well approximates that of the actual cells. Since in a physical sense the boundaries between vorticity cells are not sharply defined anyway, it is felt that the use of equivalent rectangular cells is justified, provided that the total vorticity of the system is preserved. This is the case since the areas of the actual and substitute cells are identical.

As a result of this construction, it is now possible to integrate over the equivalent cell the expression for the induced velocity. Following a procedure which was inspired by the work of Hess and Smith,[3] an exact result is obtained if ω is assumed to be constant over the cell.

A typical substitute rectangular cell is shown in Fig. 3. The x and y axes conform to the Cartesian system already introduced in Part I, with x running parallel to the airfoil chord.

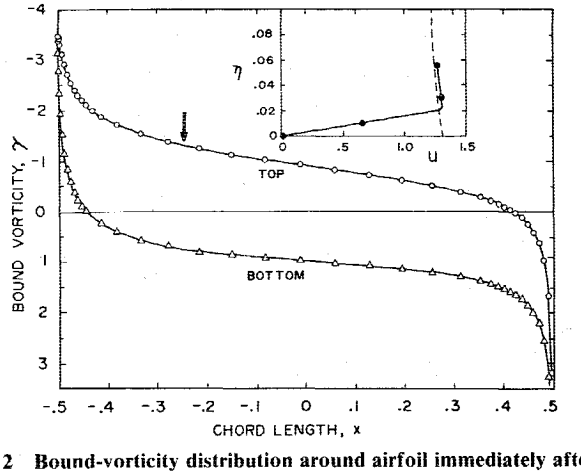

Fig. 2 Bound-vorticity distribution around airfoil immediately after impulsive acceleration for $\alpha = 30$ deg.

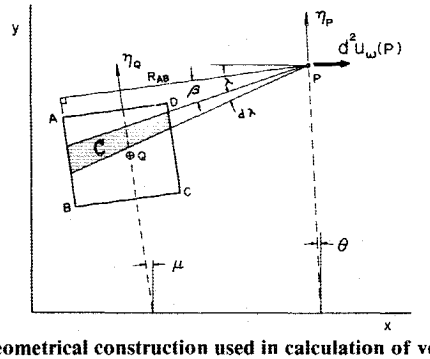

Fig. 3 Geometrical construction used in calculation of velocity from Biot-Savart law.

The dashed lines labelled η_P and η_Q are normal to the airfoil surface, and μ and θ are the slope-angles of the tangents to the airfoil surface. We now consider the contribution of the differential shaded region of vorticity da to the perturbation velocity component at P. This is given by

$$d^2u_\omega(P) = \frac{-\omega}{2\pi}\left[\frac{\sin(\lambda-\theta)}{r}\right]da \tag{5}$$

which is equivalent to Eq. (1a) given in Part I.

Observe that the shaded region is actually the difference of two infinitesimal triangular regions, with bases on AB and CD. In fact, the entire rectangular region $ABCD$ is composed of sums and differences of four triangular regions, with a common apex at P, and bases conforming to the four sides of the rectangle. Therefore, Eq. (5) can be integrated over each of the triangular regions, and the results then summed. However, the algebraic sign of each contribution must be carefully observed. Proceeding around the rectangle from A to D and back again to A, contributions are treated as positive if λ increases in the counterclockwise direction, and negative for the reverse situation. For example, the contribution from PAB is positive, whereas that from PDA is negative.

For a single triangular region, such as PAB, one first writes $da = rdrd\lambda$, and Eq. (5) is integrated with respect to r from 0 to its value on AB. If R_{AB} denotes the perpendicular distance between P and AB, one can write

$$\int_{PAB}\frac{\sin(\lambda-\theta)}{r}da = R_{AB}\int_{\lambda_A}^{\lambda_B}\frac{\sin(\lambda-\theta)}{\cos\beta}d\lambda \tag{6}$$

Note that $\lambda=\beta+\mu$ and $d\lambda=d\beta$. The sine function can be expanded and the final integration performed from β_A to β_B. One obtains

$$\int_{PAB}\frac{\sin(\lambda-\theta)}{r}da = R_{AB}\left[(\beta_B-\beta_A)\sin(\mu-\theta) + \cos(\mu-\theta)\ln\left(\frac{\cos\beta_A}{\cos\beta_B}\right)\right] \tag{7}$$

Results for the remaining three triangular regions can be obtained in a similar manner. When these results are summed and multiplied by $-\omega/2\pi$, a semianalytical approximation to the integral of Eq. (5) over a fluid cell is obtained.

The foregoing procedure is believed to be quite accurate, but it is nevertheless time consuming to apply computationally. Therefore, when the distance r_{PQ} was sufficiently large, Eq. (5) was applied directly without integration. That is, the vorticity within the rectangular region of area ΔA was treated as a point vortex of strength $\omega\cdot\Delta A$ located at Q. It was verified that when r_{PQ} was more than five times the diagonal dimension of the fluid cell, this approximation yielded results which were within a fraction of a percent of those obtained using the more nearly exact integrations.

The contribution to the perturbation velocity at P due to the bound vorticity was computed in an analogous way. The vorticity γ_m was taken to be constant over the incremental length of the airfoil ΔS_m, which was assumed to be a straight line. An analytical expression analogous to Eq. (7) was then obtained for the incremental velocity upon integration of the Biot-Savart law over ΔS_m. When the distance between a surface point and the point P in the fluid was greater than five times ΔS_m, the vortex element was treated as a point vortex with strength $\gamma_m\Delta S_m$. This treatment is similar to that previously described.

The sum of all of the perturbation velocities from the bound and free vorticity were than added to the contribution from the onset flow. In this manner, the u components of velocity were obtained at the "vertical" control surfaces of each of the 800 fluid cells. The v components were then calculated using the continuity equation, starting with the zero values along the airfoil surface. Datum values at points along the x axis behind the trailing edge were also needed at each time level. These were obtained from an application of the Biot-Savart law. This required integrations analogous to those already described in connection with Eq. (5), but with $\sin(\lambda-\theta)$ replaced by $\cos(\lambda-\theta)$.

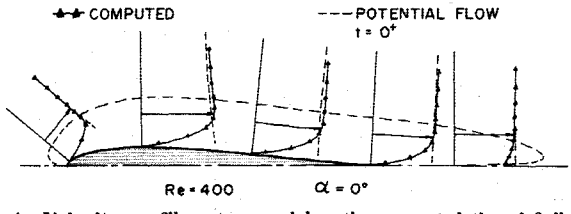

Fig. 4 Velocity profiles at several locations around the airfoil for $t=0.28$.

Results and Discussion

Calculations were performed for a fixed Reynolds number of 400 and angles of attack equal to 0 and 30 deg. These parameters correspond with those used in the flat-plate problem studied by Schmall and Kinney.[4]

A fixed time step Δt was chosen according to the criteria presented in Part I. This requires that $\Delta t \lesssim Re\delta^2/10$, where the thickness δ is the height of the control volumes adjacent to the airfoil surface. In this work, $\delta=\Delta\eta_0=0.02$. Thus Δt must be less than 0.016. A conservative value of $\Delta t=0.005$ was selected. This insured that the Courant numbers, $u\Delta t/\Delta\xi$ and $v\Delta t/\Delta\eta$, were less than or equal to approximately 0.7, and the explicit numerical method was stable.

Airfoil at Zero Angle of Attack

A composite picture showing the velocity profiles at selected stations around the airfoil is given in Fig. 4. The results were obtained after 56 time steps and show the development of the viscous layer about the airfoil and in the wake region. Although calculations were performed throughout the entire flowfield, only the results in the upper half-plane are shown, since it was found that the flow was indeed symmetrical. The approximate extent of the vorticity layer ($\omega=-0.1$) is indicated by the contour running between the leading and trailing edges. The dashed velocity curves show the potential-flow velocity distribution immediately after the impulsive acceleration.

The temporal development of the pressure coefficient is shown in Fig. 5. This was computed using Eq. (16) of Part I as follows:

$$C_P(S) \equiv \frac{P(S)-P^*}{\rho U^2/2} = \frac{2}{\Delta t}\int_{TE}^{S}\gamma dS = \frac{2}{\Delta t}\sum_{m=1}^{M}\gamma_m\Delta S_m \tag{8}$$

where the reference pressure P^* was taken to be the value at the trailing edge (TE). The time value assigned to the pressure distribution was taken to be midway through a time increment.

Since C_P was obtained from a direct calculation using the γ distribution, the values are shown as single points.‡ For the earliest time, $t=0.0075$, a favorable streamwise pressure gradient exists everywhere along the airfoil, as indicated by the negative slope of the C_P curve. At later times, however, the pressure gradient becomes unfavorable over most of the airfoil. At the last time shown, the pressure over the thickest portion of the airfoil is less than that at the trailing edge. This indicates that as the velocity boundary layer develops, the

‡At zero angle of attack, the γ distribution was sufficiently smooth that only 40 vortex points were used to represent the outline of the airfoil.

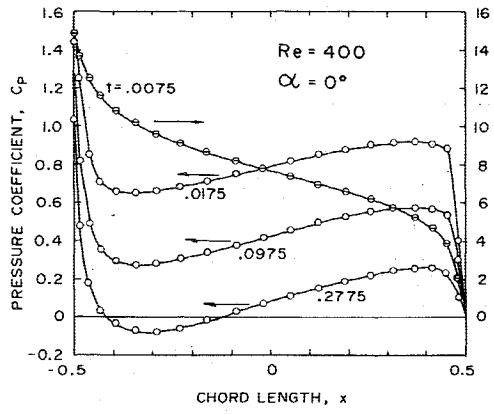

Fig. 5 Development of pressure coefficient with time.

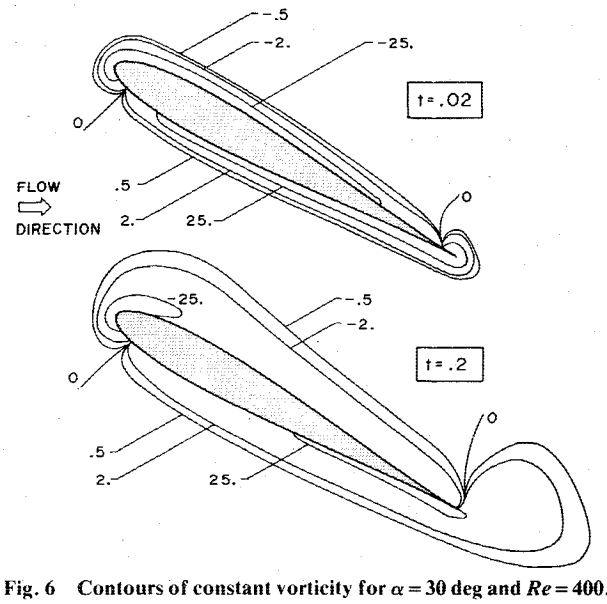

Fig. 6 Contours of constant vorticity for $\alpha = 30$ deg and $Re = 400$.

drag due to pressure decreases sharply. Although not shown here, the drag due to both pressure and friction was calculated, and the latter was found to be completely dominating. More extensive results are given in Ref. 2.

Airfoil at Angle of Attack

Contours of constant vorticity are shown in Fig. 6 at two different instances in time. The intersection of the zero-vorticity curves with the airfoil surface give the points of vanishing wall shear. The intersection point on the lower surface near the leading edge is practically stationary, whereas that on the upper surface moves rapidly toward the trailing edge. The development of the starting vortex at the trailing edge is very evident, and the region of large negative vorticity near the leading edge is believed to be a precursor to the onset of leading-edge separation. However, the calculations were not carried beyond $t = 0.2$.

Representative velocity profiles are shown in Fig. 7 for $t = 0.2$. The dashed curves give the potential-flow velocity distributions immediately after the impulsive acceleration. Although the airfoil has moved only 0.2 of its chord length, it is clear that the flow is momentarily leaving smoothly from the trailing edge. A more detailed picture of the velocity-field development with time on the upper surface near the trailing edge is given in Fig. 8. These curves exhibit the same general trends found in Ref. 4. At $t = 0.03$, the fluid adjacent to the airfoil is flowing in the mainstream direction, whereas that at a slightly higher elevation is flowing in the opposite direction. This is characteristic of the flow pattern associated with

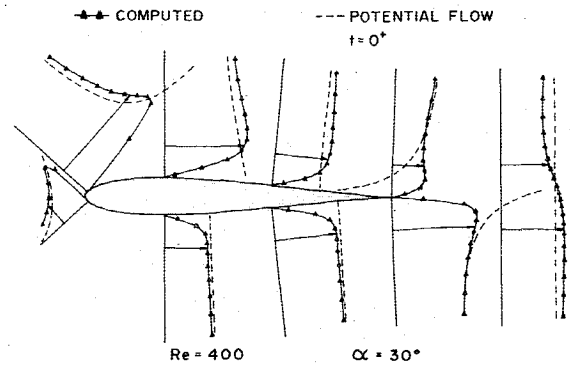

Fig. 7 Velocity profiles at several locations around the airfoil for $t = 0.20$.

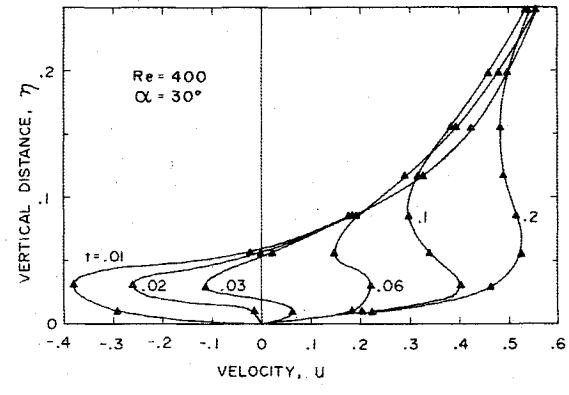

Fig. 8 Transient development of velocity profiles on the upper surface near the trailing edge ($x = 0.475$).

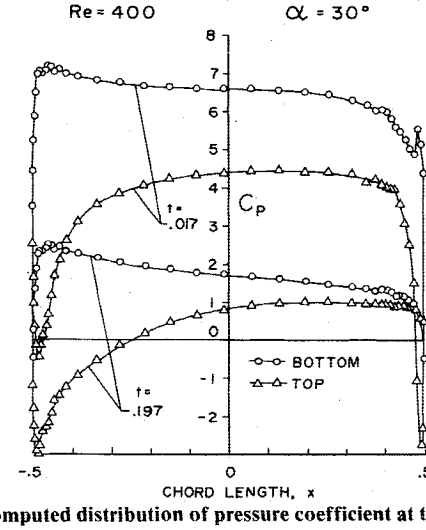

Fig. 9 Computed distribution of pressure coefficient at two different times.

downstream-moving unsteady-flow separation, as discussed in the summary paper by Sears and Telionis.[5]

The distribution of the pressure coefficient at two fixed times is shown in Fig. 9. For these calculations at $\alpha = 30$ deg, the full 80 surface points were used for calculation of the bound-vorticity distribution over the airfoil. The values of C_P computed numerically from Eq. (8) for each surface point are shown, and the results were not smoothed in any way. The behavior is as expected, and on the whole the variation in pressure is regular and smooth. The only exception occurs at two isolated points on the bottom surface of the airfoil near the trailing edge soon after the airfoil is set into motion. This may be due to numerical inaccuracies caused by the cusped

trailing edge, particularly at early times when the flow must turn the corner and proceed back along the upper surface. The flow near a cusped trailing edge is extremely difficult to model numerically, and the precision of the present results is believed to be quite good.

Concluding Remarks

A procedure has been presented for calculating the unsteady two-dimensional flow produced by an airfoil moving through a viscous fluid. In broad terms, it is a procedure which closely parallels that used in more classical unsteady airfoil theories (see Ref. 5 of Part I).

As in the classical theory, the result of most practical importance is the pressure distribution on the airfoil surface. Interestingly in both instances the pressure distribution is obtained from the bound-vorticity distribution on the airfoil. However, the dynamical procedure used to calculate it is quite different. In the classical theory, the bound vorticity is simply related to the surface slip-velocity of the fluid. This is then substituted into the Bernoulli equation in order to determine the pressure gradient. In the present approach, the bound-vorticity distribution determines the flux of total vorticity from the airfoil surface into the fluid. This is then substituted into the viscous-flow momentum equation (along with the no-slip condition) in order to determine the pressure gradient [see Eqs. (15) and (16) of Part I].

The effect of the viscous layer (boundary layers plus wake) on the pressure distribution is accounted for through the term u_ω in Eq. (2). This is the counterpart of the "wake integral" which appears in the classical theory. Further, the interaction between the boundary-layer and wake regions is fully accounted for through the use of the Biot-Savart law to obtain the velocity field in the fluid.

The principle of the conservation of total vorticity has been incorporated into the present analysis, this being the counterpart of the Kutta-Joukowski condition used in the classical theories. The enforcement of this principle insures that the bound-vorticity distribution is nonambiguous, while at the same time rendering the pressure distribution single-valued on the airfoil.

The present formulation constitutes a marriage between the classical inviscid-flow theories and the more modern boundary-layer approaches. Compared to stream function methods, which have been evolving over the past two decades, it is in the very earliest stages of development. It does appear to have great potential for treating a wide variety of unsteady viscous-flow problems, but much more experience is needed before the specific advantages or disadvantages are known.

Acknowledgments

This work was supported by the National Science Foundation under Grant No. ENG73-03855 A01. The revised manuscript was prepared while the second author was on leave to the DFVLR-AVA, Institut für Aeroelastik, Göttingen, Germany. The financial support of the Alexander von Humboldt Foundation, Bonn, Germany, is gratefully acknowledged.

References

[1] Kinney, R. B. and Cielak, Z. M., "Analysis of Unsteady Viscous Flow Past an Airfoil: Part I—Theoretical Development," *AIAA Journal*, Vol. 15, Dec. 1977, pp. 1714-1719.

[2] Cielak, Z. M., "Vorticity-Oriented Analysis of Viscous Flow over a Two-Dimensional Airfoil," Ph.D. thesis, Univ. of Arizona, Tucson, Ariz., 1976.

[3] Hess, J. L. and Smith, A. M. O., "Calculation of Potential Flow About Arbitrary Bodies," *Progress in Aeronautical Sciences*, Vol. 8, edited by D. Küchemann, Pergamon Press, New York, 1967.

[4] Schmall, R. A. and Kinney, R. B., "Numerical Study of Unsteady Viscous Flow past a Lifting Plate," *AIAA Journal*, Vol. 12, Nov. 1974, pp. 1566-1573.

[5] Sears, W. R. and Telionis, D. P., "Boundary-Layer Separation in Unsteady Flow," *SIAM Journal on Applied Mathematics*, Vol. 28, Jan. 1975, pp. 215-235.